Aerodynamic Analysis of Civil Aero-Engine Exhaust Systems using Computational Fluid Dynamics

John J. Otter[1], Ioannis Goulos[2] David G. MacManus[3]
Cranfield University, Bedford, United Kingdom, MK43 0AL

Michal Slaby[4]
Rolls-Royce plc., Derby, United Kingdom, DE24 8BJ

As the specific thrust of civil aero-engines reduces, the aerodynamic performance of the exhaust system will become of paramount importance in the drive to reduce engine fuel burn. This paper presents an aerodynamic analysis of civil aero-engine exhaust systems through the use of Reynolds Averaged Navier-Stokes Computational Fluid Dynamics . Two different numerical approaches were implemented and the numerical predictions were compared to measured data from an experimental high-bypass ratio separate-jet exhaust system. Over a fan nozzle pressure ratio range from 1.4 to 2.6, a comparison was drawn between values of thrust coefficient calculated numerically and values obtained from experimental measurements. In addition to the validation of numerical approaches, the effects of freestream Mach number and extraction ratio on the aerodynamic behavior of the exhaust system have been quantified and correlated to fundamental aerodynamic parameters.

---

[1] Ph.D Student, Propulsion Engineering Centre, Building 52.

[2] Lecturer in Propulsion Integration, Propulsion Engineering Centre. Building 52.

[3] Professor of Propulsion Aerodynamics and Installations, Propulsion Engineering Centre, Building 52, Member AIAA.

[4] Aerothermal Engineer, Installation Aerodynamics, Rolls-Royce plc.

Nomenclature

Roman Symbols

a_n	Constant in specific heat calculation
A	Area (m²)
A^*/A	Isentropic area ratio (dimensionless)
c_p	Specific heat capacity (J/kgK)
C_D^{Bypass}	Bypass discharge coefficient (dimensionless)
C_D^{Core}	Core discharge coefficient (dimensionless)
C_{Fx}	Axial force coefficient (dimensionless)
C_V^*	Modified thrust coefficient (dimensionless)
$CNPR_e$	Effective core nozzle pressure ratio (dimensionless)
$CNPR_p$	Prescribed core nozzle pressure ratio (dimensionless)
dS	Elemental surface area (m²)
dA	Elemental inlet area (m²)
D	Maximum fan cowl diameter (m)
D_{Domain}	Diameter of hemispherical domain (m)
ER	Extraction ratio (dimensionless)
$FNPR_e$	Effective fan nozzle pressure ratio (dimensionless)
$FNPR_p$	Prescribed fan nozzle pressure ratio (dimensionless)
F_G^x	Axial gauge stream force (N)
GPF	Gross propulsive force (N)
GPF^*	Modified gross propulsive force (N)
k	Turbulent kinetic energy (J/kg)
K	Critical flow factor (kg K$^{0.5}$ N^{-1} s^{-1})
$\dot{m}$	Mass flow rate (kg/s)
M_{inf}	Freestream Mach number (dimensionless)
M_{isen}	Isentropic mach number (dimensionless)
M_w	Molecular weight of air
N	Number of data points (dimensionless)
NPR_e	Effective nozzle pressure ratio (dimensionless)
NPR_p	Prescribed nozzle pressure ratio (dimensionless)
p	Static Pressure
P	Total Pressure
R^2	Coefficient of determination (dimensionless)
$RMSD$	Root mean squared distance (percentage)
T	Static temperature (K)
T_0	Total temperature (K)
u	Velocity (m/s)
y	Wall distance (m)
y^+	Dimensionless wall distance (dimensionless)

Greek Symbols

α	Local surface angle (degrees)
γ	Ratio of specific heats (dimensionless)
ΔC	Change in non-dimensional coefficient (%)
θ	Force in the thrust domain (N)
ϕ	Force in the drag domain (N)
ζ	Constant in core discharge coefficient model (dimensionless)
λ	Exponent weight factor in core discharge coefficient model (dimensionless)
ξ	Exponent in core discharge coefficient model (dimensionless)
ρ	Density (kg/m³)
μ	Dynamic viscosity (kg/ms)
τ_w	Wall shear stress (N/m²)
τ_x	Axial wall shear stress (N/m²)

ω	Specific dissipation (m^2/s^{3}kg)
Ω	Absolute value of vorticity (1/s)
μ_t	Eddy viscosity
ψ	Constant in $k - \omega$ SST turbulence model

Subscripts and Superscripts

13	Bypass inlet station
19	Bypass exit station
$19 - te$	Fan cowl trailing edge
7	Core inlet station
9	Core exit station
$\sim$	Mass-averaged value
—	Time averaged component
atm	Atmospheric
BP	Bypass nozzle
$Bypass$	Bypass nozzle
cc	External Core cowl
CFD	Computed with CFD
$Core$	Core nozzle
CR	Core nozzle
cp	External Core plug
$crtical$	At sonic conditions
Exp	From experimental measurements
Fit	From curve fit
$Ideal$	Ideal isentropic conditions
$inlet$	Inlet of a nozzle
$pylon - wet$	The part of the pylon which the bypass jet washes over
$pylon - dry$	Part of the pylon which the bypass jet does not wash over
$throat$	Geometric nozzle throat
x	Axial

Acronyms

CFD	Computational Fluid Dynamics
DSFRN	Dual Separate Flow Reference Nozzle
GCI	Grid Convergence Index
GEMINI	Geometric Engine Modeller Including Nozzle Installation
PAW	Propulsion Aerodynamics Workshop
RANS	Reynolds Average Navier-Stokes
SFC	Specific Fuel Consumption

I.Introduction

A. Background

The reduction of engine specific fuel consumption (SFC) is a major impetus in the development of aero-engines and the aerodynamic performance of the exhaust system is fundamental to this drive. In order to increase propulsive efficiency and hence reduce SFC future engines are expected to operate with high bypass ratios [1], low Fan Pressure Ratios and low specific thrust relative to current engines which are in service [2]. For a given engine net thrust, this combination of increased bypass ratio and reduced specific thrust will result in a larger ratio between the gross and net engine thrust. For example, an increase in bypass ratio from 11 to 16 leads to an approximate increase of the gross to net ratio from 3 to 4 [3]. This occurs as a higher gross thrust is required to compensate for the increased inlet momentum drag which arises from a greater overall engine mass flow. Consequently, the overall effect of losses in the exhaust system, along with the impact on SFC, increases as this ratio of gross to net thrust increases. As such, overall engine efficiency for future engine configurations will become more dependent upon the aerodynamic performance of the exhaust system. Therefore, it is clear that greater emphasis should be placed on the design of the exhaust system to ensure that, upon installation, the proposed benefits of high bypass ratio engines are realized.

In this work, the exhaust system refers to the bypass duct and nozzle, core duct and nozzle, core cowl and core plug, pylon, and bifurcations (shown in Fig. 1). The primary purpose of an exhaust nozzle is to accelerate the airflow to a high velocity in order to generate thrust with minimal total pressure losses [4]. The aerodynamic performance of an exhaust system is characterized by two non-dimensional performance metrics: the thrust and discharge coefficients. The thrust coefficient accounts for the thrust lost in the exhaust system due to non-isentropic flow features. The major mechanisms for thrust loss arise due to the formation of shear layers between the freestream, bypass stream and core streams, the shear stress on the nozzle and afterbody walls, and shock waves on the nozzle afterbodies. The discharge coefficient is a measure of the reduction in nozzle mass flow due to total pressure losses, flow blockage due to boundary layer growth, and suppression due to the external flow conditions. In addition to thrust generation, the exhaust system ensures the operability of the engine by providing the desired fan and low pressure turbine exit flow capacities [5]. If the required flow capacities are not catered for by the exhaust system, then the engine may be forced to operate at off-design conditions. In order to compensate for any incompatible mass flows, the nozzle throat areas are often increased or decreased accordingly. However, detailed knowledge of exhaust

system performance early in the design process can ensure that the desired engine operating point can be achieved without substantial modifications to the nozzle design.

B. Aero-Engine Exhaust Aerodynamics

The prescribed nozzle pressure ratio (NPR_p), is defined by the ratio of the total pressure at the inlet of the nozzle (P) to the ambient static pressure (p_{atm}), Eq. (1) . For a dual stream exhaust system, Fig. 1, a nominal NPR_p is defined for both core ($CNPR_p$) and bypass nozzles ($FNPR_p$) respectively, Eq. (2) and (3).

$$NPR_p = \frac{P}{p_{atm}} \tag{1}$$

$$FNPR_p = \frac{P_{13}}{p_{atm}} \tag{2}$$

$$CNPR_p = \frac{P_7}{p_{atm}} \tag{3}$$

However, due to the effect of external flow conditions, the local base pressure into which the nozzle discharges may not be the same as the ambient static pressure [6,7]. This is referred to as flow suppression and the effect becomes greater at low NPR_p [6]. For the bypass nozzle, suppression can be caused by higher than ambient static pressure in the region of the trailing edge of the fan cowl [7]. For the core nozzle, this suppression arises due to the fan flow being directed towards the core exhaust [8] and due to the bypass jet preventing the core jet from expanding to the ambient static pressure.

During cruise conditions the bypass nozzle will operate under choked conditions and as a result the nozzle mass flow rate is insensitive to downstream flow conditions. On the contrary, the core nozzle typically operates under unchoked conditions [3] and is therefore more sensitive to the external flow conditions. For example, the core discharge coefficient can vary up to 6% across a typical engine cruise schedule [9]. Very few studies of flow suppression have been published in the open literature. The most relevant investigation for a separate-jet exhaust system was presented by Odbert [8]. This investigation consisted of measurements of both fan and core discharge coefficients for a convergent bypass nozzle and convergent-divergent core nozzle. Results were reported over a $FNPR_p$ range from 1.1 to 3.0, extraction ratios (ER), as defined in Eq. (4), of 1.0, 1.32, 1.37, 1.42 and 1.52 with all tests completed under quiescent freestream flow conditions [8]. For these experiments the bypass nozzle discharge

coefficient was shown to be invariant with ER [8]. Furthermore, it was shown that at an ER of 1 the suppression of the core was negligible when the core nozzle operates at choked conditions. At a typical cruise subcritical $CNPR_p$ of 1.5 [3], and compared with measurements of the isolated core nozzle, the core discharge coefficient was reduced by 6% and 14% at ERs of 1 and 1.4 respectively. However, no investigation was made into the impact of freestream Mach number on the flow suppression of either stream.

$$ER = \frac{P_{13}}{P_7}$$

(4)

The variation of the core nozzle discharge coefficient has a direct impact on the design considerations for the core nozzle. Therefore, any reductions in the core discharge coefficient must be corrected by an increase in the throat area in order to meet the desired flow capacity requirements. In terms of thrust coefficient, a variation of up to 1.5% between static and flight conditions can be expected [9]. A study completed by Geyr [7] concluded that above Mach numbers of 0.25 the thrust coefficient is dependent on the freestream Mach number with the exhaust afterbody and post-exit forces found to be the largest contributors to the variation of thrust with freestream Mach number. As nozzle performance metrics are commonly assessed at static conditions there is a necessity to quantify the impact of external flow conditions on the nozzle performance metrics and account for these effects with a robust design methodology.

C. Computational Methods for the Calculation of Exhaust System Flows

Computational Fluid Dynamics (CFD) is one of the primary tools used in the design and analysis of aero-engine exhaust systems [10] with an application of three-dimensional Reynolds Average Navier-Stokes (RANS) CFD to commercial turbofan exhaust system geometries undertaken by Keith et al. [11] and Abdol-Hamid et al. [12]. The computational results presented by Abdol-Hamid et al. for a separate-jet exhaust system were found to be within 0.6% and 0.2% of experimental data for the thrust coefficient and fan discharge coefficient respectively. Subsequently, there have been numerous investigations within the literature on the use of RANS CFD for the calculation of aerodynamic performance metrics for civil separate-jet nozzles [13,14,15,16]. Moreover, due to the high temperatures present in the core jet [13], research has been undertaken in order to assess the limitations of RANS CFD for predicting heated nozzle flows [17,18]. The development of a temperature corrected turbulence

model has been shown to provide more accurate prediction of jet flows which feature high temperature gradients compared to results obtained from the standard k-epsilon turbulence model [18] compared to results from standard two-equation turbulence models. In addition to the assessment of exhaust system aerodynamic performance, CFD has also been applied to investigate and reduce sources of noise that arise from the exhaust system [10,19].

The advent of the Propulsion Aerodynamics Workshop (PAW) [20] has led to a recent increase in the body of research focused on the application of RANS CFD to the prediction of exhaust nozzle aerodynamic performance [21,22,23,24,25]. The second PAW was focused on the numerical simulation of a separate-jet exhaust system known as the Dual Separate Flow Reference Nozzle (DSFRN) [26]. The nozzle used in the second PAW was developed by the AIAA Ground Testing Technical Committee Dual Flow Reference Nozzle Working Group [**Error! Bookmark not defined.**]. Experimental nozzle rig tests for the DSFRN were carried out with quiescent freestream conditions over a $FNPR_p$ range from 1.4 to 2.6 with a constant ER of 1.2. Based on the average values obtained by participants of the workshop [21, 25], axial thrust coefficient was calculated to within 0.6% of experiment measurements [**Error! Bookmark not defined.**] for a $FNPR_p$ ratio range of 1.4 to 2.6. Similarly, across the same $FNPR_p$ range the core and fan discharge coefficients were calculated to within 1.5% and 0.8% respectively [21]. Based on the gross to net thrust ratios of approximately 3 and 4 for engines with BPR of 11 and 16 [3], a discrepancy of 0.6% in thrust coefficient will result in a concomitant discrepancy in SFC of approximately 1.8% and 2.4% respectively. Evidently, advancements in the aerodynamic modeling of separate-jet exhausts are required in order to accurately predict the aerodynamic behavior of separate-jet exhausts and hence provide accurate estimates of engine SFC.

D. Scope of the Present Work

Based upon the preceding discussion, it is clear that the aerodynamic performance of separate-jet exhaust systems is of paramount importance to the success of future high BPR aero-engines. It is imperative that the effects of flight Mach number on nozzle performance are considered in the preliminary design stages of an engine development program. However, a systemic investigation into the effects of flight Mach number and extraction ratio on exhaust nozzle performance does not exist in the current literature. This dearth of knowledge is addressed through a computational study of a high-bypass separate-jet exhaust system across a range of flight Mach numbers. This investigation is supported by a novel approach for quantifying changes to the nozzle operating point due to

freestream conditions. Furthermore, the underlying aerodynamic mechanisms which govern the variation of nozzle performance metrics in flight are identified.

In order to investigate exhaust system performance at the preliminary design phase, practical and robust computational approaches to predict the aerodynamic performance of separate-jet exhausts must be developed. Although methods for the prediction of separate-jet exhaust system performance have been documented, they have not been shown to accurately predict nozzle thrust and discharge coefficients over a range of operating conditions. This work presents a significant development in the use of CFD for the prediction of nozzle performance metrics for both 3D and 2D axisymmetric configurations. Specifically, a numerical approach for the prediction of modern high-bypass ratio separate-jet exhaust system aerodynamic performance has been investigated and validated against experimental data.

II.Methodology

The methodology based upon the scope of work can be split into five sections. Firstly, a brief summary of the DSFRN experimental set-up is given. This is then followed by the definition of the key non-dimensional metrics which quantify the aerodynamic performance of separate-jet exhaust systems. To close the performance accounting procedure the thrust and drag bookkeeping methods used with this work are discussed. Furthermore, an overview of the computational approach is demonstrated. Finally, the parameters required to sufficiently quantify flow suppression are defined and the methods for the quantification and correlation of the nozzle performance metrics are given.

A. Dual Flow Stream Reference Nozzle Experimental Set-up

The DSFRN model was designed to be representative of a commercial transport turbofan engine with a bypass ratio of the order of 10 to 12 [**Error! Bookmark not defined.**]. The model consisted of two flow streams, one to simulate the flow from a fan stream and one to simulate the flow from the core engine, Fig. 1. The fan stream contained two bifurcation sections and the core duct contained a plug with support struts. In addition, both ducts were attached to convergent nozzles at the duct exit. A pylon is present and attached to the upper surface of the fan cowl. Only the fan stream flows over this pylon and the core stream discharges onto the heat shield underneath the pylon. The air flow upstream of the nozzle ducts was throttled and then split into the core and fan streams with the

mass flow through the core measured to determine the mass flow rate split. The thrust generated from the nozzle was measured via a three-component strain gauge force balance [**Error! Bookmark not defined.**]. To obtain an experimental nozzle performance characteristic for the DSFRN, the $FNPR_p$ and $CNPR_p$ were varied via the total pressure of the respective stream. The DSFRN discharged into a quiescent atmosphere at static ambient conditions. A total of nine $FNPR_p$ were investigated with a constant ER of 1.2. The total temperature at the inlet of both the core and fan streams was the same and remained constant across the range of the $FNPR_p$ [**Error! Bookmark not defined.**]. It should be noted that although the DSFRN experiment was completed with cold jets, with bypass and core total temperatures of approximately 300K, in practice the core jet often has a much higher total temperature, typically in the order of 826K [13]. When operating at higher total temperatures variations to the gas properties will occur and afterbody drag, jet plume shapes and jet entrainment are known to be dependent on the ratio of specific heats, gas constant and total temperature [27].

Total pressure rakes were distributed radially and azimuthally at both the core and bypass duct charging planes. The azimuthal locations of each set of rakes was consistent between the two ducts with azimuthal angles of 45º, 135º, 225º and 315º. Each of the rakes in the bypass duct comprised of twelve radial probes and six probes were used for each rake in the core duct. An additional 12 total pressure pitot probes were positioned in the bypass stream close to the inner and outer wall surfaces to measure the boundary layer. Each set of boundary layer probes were staggered azimuthally. In addition to total pressure rakes, four static pressure measurements were taken at the charging plane for both the bypass and core stations at azimuthal angles of 55º, 145º, 235º and 325º.

B. Exhaust Performance Accounting

This section outlines the definition of the nozzle performance metrics of interest to this study. The experimental definitions for the discharge and thrust coefficient for the DSFRN wind tunnel tests were defined by Mikkelsen et al.[**Error! Bookmark not defined.**]. The non-dimensional coefficients were defined such that a direct comparison between the experimental and computational coefficients could be made.

Discharge Coefficient

The discharge coefficient is defined as the ratio of the actual nozzle mass flow to the ideal mass flow which would flow through the nozzle under isentropic conditions with fixed inlet total pressure and temperature. The ideal mass flow rate, Eq. ((5)), is a function of the NPR_p of the respective stream, total pressure (P), total temperature (T_0), gas constant (R) and ratio of specific heats (γ). Note that for cases where NPR_p is greater than the critical nozzle pressure ratio (NPR_{crit} defined in Eq. (6)) the value of NPR_{crit} is used to compute the ideal mass flow in Eq. ((5)). A discharge coefficient is defined for both the core and fan streams as the ratio of the mass flow to the ideal mass flow, Eq.(7)**Error! Reference source not found.Error! Reference source not found.**. The $CNPR_p$ was used in Eq.**Error! Reference source not found.** (5) to determine the ideal core mass flow rate and similarly the $FNPR_p$ is used for the ideal fan mass flow rate.

$$\dot{m}^{Ideal} = PA_{throat}\left(\frac{1}{NPR_p}\right)^{\frac{1}{\gamma}}\sqrt{\frac{2\gamma}{(\gamma-1)RT_0}\left(1-\left(\frac{1}{NPR_p}\right)^{\frac{\gamma-1}{\gamma}}\right)} \tag{5}$$

$$NPR_{crit} = \left(\frac{\gamma+1}{2}\right)^{\frac{\gamma-1}{\gamma}} \tag{6}$$

$$C_D^{Bypass} = \frac{\dot{m}_{Bypass}}{\dot{m}_{Bypass}^{Ideal}}; C_D^{Core} = \frac{\dot{m}_{Core}}{\dot{m}_{Core}^{Ideal}} \tag{7}$$

Thrust Coefficients

The thrust coefficient is the ratio of the actual thrust generated from a nozzle to the thrust which would be obtained if both the core and fan streams were to expand isentropically to the atmospheric static pressure. The gauge stream force at the exit of a nozzle is a sum of the axial momentum ($\dot{m}u_x$), and gauge pressure, ($p - p_{atm}$), which acts over the axial nozzle exit area (A_x), Eq. (8). For an ideal fully expanded nozzle the gauge pressure will always be zero at the nozzle exit and therefore the ideal thrust is only dependent upon the nozzle exit velocity. The ideal fully expanded velocity at the exit of the nozzle is given by Eq.(9). The ideal thrust of the entire exhaust system is given as the sum of the ideal thrusts for both the core and bypass nozzle, Eq. (10). In this definition of the ideal thrust, the measured mass flows of the core and fan streams are used. This is shown by the use of the bypass and core discharge coefficients in Eq. **Error! Reference source not found.**(10)**Error! Reference source not found.**. The experimental nozzle coefficients reported by Mikkelsen et al. were calculated based on an assumed constant

value of γ equal to 1.4 and as such this value has also been used to obtain the ideal mass flow rates and velocities in Eqs. (5) and (10). However, it should be noted that the computations presented within this work were undertaken with γ as a function of static temperature (as defined by Eq.(28)).

$$F_G^x = \dot{m}u_x + (p - p_{atm})A_x \tag{8}$$

$$u^{Ideal} = \sqrt{\frac{2\gamma R T_0}{(\gamma - 1)}\left(1 - \left(\frac{1}{NPR_p}\right)^{\frac{\gamma-1}{\gamma}}\right)} \tag{9}$$

$$\sum \dot{m}\,u^{Ideal} = C_D^{Bypass}\dot{m}_{Bypass}u_{Bypass}^{Ideal} + C_D^{Core}\dot{m}_{Core}u_{Core}^{Ideal} \tag{10}$$

The exhaust performance accounting system used within this work is based on a well-established Thrust and Drag Bookkeeping (TDB) system [28]. A force is defined as a thrust if it lies within the engine's streamtube [28] (Fig. 1) and is denoted with the symbol θ. Forces outside the engine streamtube are defined as drag and are denoted with the symbol ϕ. The forces on the fan cowl and part of the pylon will lie in the drag domain and although these forces will be small when there is no freestream flow, significant forces arise when the freestream Mach number is non-zero. The axial force measured by the experimental strain gauge included all of the forces on the DSFRN and consequently is not a thrust, but rather a rearward force. Therefore, within this work the experimentally measured thrust coefficient will be referred to as a force coefficient (C_{Fx}). It is defined as the experimental axial force divided by the sum of the ideal thrusts from the core and fan flows, Eq. (11).

$$C_{Fx} = \frac{F_{G13}^x + F_{G7}^x + \sum(\phi^x + \theta^x)}{\sum \dot{m}\,u^{Ideal}} \tag{11}$$

The modified thrust coefficient (C_V^*) is the ratio of all of the forces inside the thrust streamtube to the ideal thrust, Eq. (12). This serves to quantify the efficiency of the entire nozzle system. To calculate C_V^* the force on the pylon would have to be split into two parts: $\theta_{pylon-wet}$, which lies in the thrust domain, and $\phi_{pylon-dry}$ which belongs to the drag domain (Fig. 1). However, when there is no freestream flow C_V^* is approximately equal to C_{Fx} and so C_V^* is not reported for the three-dimensional geometry. For the simplified two-dimensional geometry C_V^* is reported, as this geometry does not feature a pylon. However, from the computational results it is possible the split the pylon surface force into $\theta_{pylon-wet}$ and $\phi_{pylon-dry}$ based upon the total temperature on the pylon surface due to the fact that the freestream and bypass nozzle flows have different total temperatures.

$$C_V^* = \frac{F_{G19}^x + F_{G9}^x + \theta_{CC}^x + \theta_{CP}^x + \theta_{pylon-wet}^x}{\sum \dot{m}\, u^{Ideal}} \tag{12}$$

The force on each nozzle surface was obtained by direct integration of the pressure and viscous forces, Eq. (13), where p_{atm} is the ambient static pressure, p, is the static pressure on the surface, α is the local surface angle measured from the axial direction, τ_w is the local shear stress, and dS is the elemental surface area. The gauge stream forces for the fan and core streams were evaluated from CFD computations through the integration of the momentum and pressure terms at the inlets of the respective duct, Eq. (14). Where ρ is the fluid density, u_x is the axial velocity and dA is the elemental surface area of the inlet boundary.

$$\phi, \theta = \int_{surface} (p - p_{atm}) \sin \alpha\, dS + \int_{surface} \tau_w \cos \alpha\, dS \tag{13}$$

$$F_G^x = \int_{inlet} \rho U_x^2\, dA + \int_{inlet} (p - p_{atm})\, dA \tag{14}$$

C. Three Dimensional simulations

Grid Generation and Computational Domain

Only half of the DSFRN geometry was modelled due to the geometry being symmetrical about the x-z plane (Fig. 2a). To model the far-field flow conditions a hemispherical fluid domain was chosen and a pressure far-field boundary condition was used to simulate ambient flow conditions. The static pressure and total temperature imposed on this far-field boundary condition remained constant across the numerical simulations, with values of 98100 Pa and 289K respectively. In the experiment the DSFRN discharged into a quiescent atmosphere. However, to ensure numerical stability a non-zero free stream Mach number must be used. A value of 0.01 was found to be the lowest free stream Mach number which produced a converged solution in a practical timeframe. Freestream turbulence was controlled by specifying a turbulent viscosity ratio of 1 and a turbulent intensity of 0.1%. To quantify the effect of the computational domain on the nozzle performance metrics three different diameters for the hemispherical domain were investigated. Domains diameters of 20D, 40D and 60D were chosen where D was the maximum diameter on the DSFRN fan cowl.

Pressure inlet boundary conditions were used to model the core and fan stream inlets. The inlet total temperature implemented for both the core and fan streams was kept fixed in line with the experimental value. The fan and core total pressures were set to achieve the desired $FNPR_p$ and $CNPR_p$. Based on the guidelines derived from the PAW [26], a turbulent intensity of 5% and turbulent viscosity ratio of 1 was applied at the inlet of both the fan and core streams. The axial location of the pressure inlet boundaries was set to the axial location of the respective experimental charging plane. The experimental support sting was modelled as an inviscid wall and extended from the DSFRN fan cowl to 7D upstream (Fig. 2a). The length of this sting was kept fixed throughout the computations with no spurious pressures observed at the upstream boundary. The inviscid sting is set to have zero shear stress upon its surface, with the remainder of the nozzle surfaces modelled as adiabatic viscous no-slip walls.

The DSFRN geometry was meshed using a fully structured blocked approach with the resultant mesh designed for full boundary layer resolution such that y^+ was less than 1 across all of the aerodynamic conditions investigated with each computation inspected in order to ensure that this y^+ condition was met on all surfaces. A total of three mesh resolutions with a domain size of 60D were investigated at a $FNPR_p$ of 2.2 such that grid independency could be assessed with Richardson Extrapolation [29,30]. The first cell height remained fixed across all the meshes investigated. A $FNPR_p$ of 2.2 was chosen for the mesh refinement study as this is close to the expected operating point of future bypass nozzles [3]. The element count for the three meshes was 14.5 million, 21.2 million and 32.5 million. The mesh refinement was achieved through a uniform scaling of mesh nodes in each of the x, y and z directions. The medium mesh featured a total of 144 mesh nodes around the circumference of each nozzle. 151 nodes were distributed across the axial length of the bypass duct and similarly 110 nodes for the axial length of the core duct. In terms of the nozzle afterbodies, a total of 34 nodes were spanned across the core cowl and 28 along the external portion of the core plug. A total of 218 nodes were used between the leading edge of the upper bifurcation to the pylon trailing edge. In the radial direction, the bypass duct and wet part of the pylon featured 107 nodes and the core duct 99 nodes. Moreover, an exponential mesh law with a growth ratio of 1.2 was used for all edges which were normal to a viscous wall surface. A close up of the surface mesh for the medium mesh is shown in Fig. 2b.

Governing Equations

To evaluate the aerodynamic performance of the DSFRN, the field variables $(\tilde{e}, \tilde{u}_x, \tilde{u}_y, \tilde{u}_z, \overline{p}, k, \omega)$ were obtained through the solution of the Favre-averaged mean conservation equations for mass, momentum and energy (Eqs. (15)-(18) [31]).

$$\frac{\partial \overline{\rho}}{\partial t} + \frac{\partial (\overline{\rho} \tilde{u}_i)}{\partial x_i} = 0 \tag{15}$$

$$\frac{\partial (\overline{\rho} \tilde{u}_i)}{\partial t} + \frac{\partial (\overline{\rho} \tilde{u}_i \tilde{u}_j)}{\partial x_j} = -\frac{\partial \overline{p}}{\partial x_j} + \frac{\partial (\overline{t}_{ij} + \overline{\rho} \tau_{ij})}{\partial x_j} \tag{16}$$

$$\frac{\partial \left(\overline{\rho} \left(\tilde{e} + \frac{\tilde{u}_i \tilde{u}_i}{2} + k \right) \right)}{\partial t} + \frac{\partial \left(\overline{\rho} \tilde{u}_j \left(\tilde{h} + \frac{\tilde{u}_i \tilde{u}_i}{2} + k \right) \right)}{\partial x_j} = \frac{\partial}{\partial x_j} \left[\tilde{u}_i (\overline{t}_{ij} + \overline{\rho} \tau_{ij}) \right] \tag{17}$$

$$+ \frac{\partial}{\partial x_j} \left[\left(\frac{\mu}{Pr_L} + \frac{\mu_T}{Pr_T} \right) \frac{\partial \tilde{h}}{\partial x_j} + (\mu + \sigma_k \mu_t) \frac{\partial k}{\partial x_j} \right]$$

$$\overline{t}_{ij} = 2\mu \overline{S}_{ij}, \quad \overline{\rho} \tau_{ij} = 2\mu_T \overline{S}_{ij} - \frac{2}{3} \overline{\rho} k \delta_{ij}, \overline{S}_{ij} = S_{ij} - \frac{1}{3} \frac{\partial \tilde{u}_k}{\partial x_k} \delta_{ij} \tag{18}$$

In the above equations $\overline{t}_{ij}$ denotes the instantaneous viscous stress tensor, $\overline{\rho} \tau_{ij}$ denotes the Reynolds stress tensor, S_{ij} denotes the mean strain rate tensor, δ_{ij} denotes the Kronecker delta, μ_T denotes eddy viscosity, e denotes the specific internal energy, h denotes the specific enthalpy, Pr_L denotes the laminar Prandtl number, Pr_T denotes the turbulent Prandtl number, k denotes turbulent kinetic energy and ω denotes specific dissipation rate. For each field variable an overbar denotes a mean value and a tilde denotes mass averaged value [31]. Note that the Reynolds stress tensor is defined based on the Boussinesq approximation. The transport equations for k and ω are given by Eqs. (19) and (20) respectively based on the two equation $k - \omega$ Shear Stress Transport turbulence model of Menter [32] (Eqs. (21) - (26).

$$\frac{\partial (\overline{\rho} k)}{\partial t} + \frac{\partial (\overline{\rho} k \tilde{u}_i)}{\partial x_j} = \tau_{ij} \frac{\partial \tilde{u}_i}{\partial x_j} - \beta^* \overline{\rho} \omega k + \frac{\partial}{\partial x_j} \left[(\mu + \sigma_k \mu_T) \frac{\partial k}{\partial x_j} \right] \tag{19}$$

$$\frac{\partial (\overline{\rho} \omega)}{\partial t} + \frac{\partial (\overline{\rho} \omega \tilde{u}_i)}{\partial x_j} = \frac{\gamma}{\nu_t} \tau_{ij} \frac{\partial \tilde{u}_i}{\partial x_j} - \beta \overline{\rho} \omega^2 + \frac{\partial}{\partial x_j} \left[(\mu + \sigma_\omega \mu_T) \frac{\partial \omega}{\partial x_j} \right] + 2(1 - F_1) \rho \sigma_{\omega 2} \frac{1}{\omega} \frac{\partial k}{\partial x_j} \frac{\partial \omega}{\partial x_j} \tag{20}$$

$$\mu_T = \frac{a_1 k}{\max(a_1 \omega; \Omega F_2)}, \quad F_2 = \tanh(arg_2^2), \quad arg_2 = max \left(2 \frac{\sqrt{k}}{0.09 \omega y}; \frac{500 \nu}{y^2 \omega} \right), a_1 = 0.31 \tag{21}$$

In the above equations Ω denotes the absolute value of vorticity and y denotes dimensional wall distance. The constants, ψ, of the model are calculated from the constants ψ_1 and ψ_2 by Eqs. (22)-(24). The constants of set 1, ψ_1, are given by Eq. (25) and the constants of set 2, ψ_2, are given by Eq. (26) .

$$\psi = F_1\psi_1 + (1 - F_1)\psi_2, \; F_1 = \tanh(arg_1^4) \tag{22}$$

$$arg_1 = min\left[max\left(\frac{\sqrt{k}}{0.09\omega y};\frac{500y}{y^2\omega}\right);\frac{4\rho\sigma_{w2}k}{CD_{k\omega}y^2}\right] \tag{23}$$

$$CD_{k\omega} = max\left(2\rho\sigma_{\omega2}\frac{1}{\omega}\frac{\partial k}{\partial x_j}\frac{\partial \omega}{\partial x_j};10^{-20}\right) \tag{24}$$

$$\sigma_{k1} = 0.85, \sigma_{\omega1} = 0.5, \beta_1 = 0.075, \beta^* = 0.09, \kappa = 0.41, \gamma_1 = \beta_1/\beta^* - \sigma_{\omega1}\kappa^2/\sqrt{\beta^*} \tag{25}$$

$$\sigma_{k2} = 1.0, \sigma_{\omega2} = 0.856, \beta_2 = 0.0828, \quad \beta^* = 0.09, \kappa = 0.41, \gamma_2 = \beta_2/\beta^* - \sigma_{\omega2}\kappa^2/\sqrt{\beta^*} \tag{26}$$

The ideal gas law, Eq. (27) where R denotes the specific gas constant, was used as the equation of state to model the working fluid of air. This was used in conjunction with an 8th order polynomial expression for specific heat capacity at constant pressure (c_p) as a function of static temperature (Eq. (28) and (29) [33]). The specific heat capacity at constant volume was determined based according to $c_v = c_p - R$. Thermal conductivity (Π) was modeled according to kinetic theory, Eq. (30) from [34], where M_w denotes the molecular weight of air. The specific energy and specific enthalpy were calculated based on Eq. (31). Finally, Sutherland's law was used for the calculation of dynamic viscosity, Eq. (32) and (33) where μ_{ref} T_{ref} and S are constants [35].

$$\bar{p} = \bar{\rho}R\tilde{T} \tag{27}$$

$$c_p(\tilde{T}) = a_0 + \sum_{i=1}^{8} a_i\left(\frac{\tilde{T}}{1000}\right)^i \tag{28}$$

$$a_0 = 0.99231, a_1 = 0.236688, a_2 = -1.852148, a_3 = 6.083152, a_4 = -8.893933, \\ a_5 = 7.097112, a_6 = -3.234725, a_7 = 0.794571, a_8 = -0.081873 \tag{29}$$

$$\Pi = \frac{15}{4}\frac{R}{M_w}\mu\left[\frac{4}{15}\frac{c_pM_w}{R} + \frac{1}{3}\right] \tag{30}$$

$$\tilde{e} = c_v\tilde{T}, \tilde{h} = c_p\tilde{T} \tag{31}$$

$$\mu = \mu_{ref}\left(\frac{\tilde{T}}{T_{ref}}\right)^{1.5}\frac{T_{ref} + S}{T + S} \tag{32}$$

$$\mu_{ref} = 1.716 \; x \; 10^{-5} \; (kgms^{-1}), T_{ref} = 273.11 \; (K), S = 110.56K \tag{33}$$

Computational Method

A steady state solution of the Favre-averaged mean conservation equations was obtained via an implicit density based compressible solver [36] with time-derivative preconditioning [37]. Second order upwind spatial

discretization schemes for pressure, momentum, energy, turbulent kinetic energy and specific turbulent dissipation rate were used. Gradients were computed with Green-Gauss node based discretization [38,39]. The inviscid flux vector was evaluated with the Roe Flux-difference splitting scheme [40]. Iterative convergence was achieved through a gradual increase of the Courant–Friedrichs–Lewy number throughout the solution from 1 - 20. Residuals of velocity, continuity, energy, turbulent kinetic energy and specific turbulent dissipation rate were monitored with convergence of at least four orders of magnitude achieved. At iterative convergence, oscillations in the non-dimensional thrust and discharge coefficients were less than 0.0001.

Aerodynamic Conditions

To account for the boundary layer which forms upstream of the bypass nozzle charging plane, non-uniform inlet total pressure profiles were imposed at the inlet of the bypass nozzle. Circumferentially averaged inlet total pressure profiles at the bypass duct inlet were specified based on the available measurements. The boundary layer probes typically provided six measurements through the boundary layer. These measurements provided a useful indication of the boundary layer thickness but the resolution was ultimately too low for a thorough evaluation. The inlet total pressure profiles were constructed to match the available measurements with an additional assumption of a $1/7^{th}$ power law turbulent boundary layer profile. The overall profile at the inlet was then adjusted to ensure that the area averaged nominal total pressure was maintained. The inlet total temperature was assumed to be constant in the radial direction with a value of 294K. Furthermore, the velocity vector at the inlet was defined to be parallel to the x-axis so that no swirl or radial velocity was present at the inlet. A similar analysis could not be completed for the core nozzle as boundary layer measurements were not taken and hence uniform total pressure and total temperature profile were prescribed at inlet plane for the core nozzle flow. A total temperature of 294K was applied at core inlet plane.

D. Two Dimensional Axisymmetric Model

An axisymmetric model representative of the DSFRN was created in order to explore the nozzle performance metrics in a less computationally expensive manner and also to assess the limitations of a simplified approach. The DSFRN nozzle aerolines have axisymmetric annuli with the three-dimensional element of the geometry arising due to the pylon and bifurcation in the bypass duct and the struts in the core duct. An axisymmetric model was

constructed by taking a cut through the three-dimensional model which did not contain any bifurcation or struts. In addition to the experimental operating conditions, a range of Mach numbers and *ER*s were investigated. Three freestream Mach numbers were chosen: 0.01 which corresponds to near sea level static conditions, 0.3 which corresponds to end of take-off, and 0.85 representative of a mid-cruise condition. The total temperature of both the fan and core streams was kept the same as the experimental conditions. The freestream Mach number was altered via an increased total pressure in the far-field. This was chosen such that the total pressure at the inlet of both streams would be the same as the experimental case, hence fixing the nozzle Reynolds number at a given NPR_p. An *ER* of 1.2 was used for the DSFRN experiment with additional calculations at *ER*s of 1.3, 1.4, 1.5 and 1.6 also undertaken. The change in extraction ratio was achieved by altering the core nozzle pressure over a range of $FNPR_p$ from 1.6 to 2.6.

The computational domain consisted of a hemispherical far-field with a diameter of 60D and an inviscid sting which extends 7D upstream of the DSFRN (Fig. 3a). The turbulence model, discretization scheme, flux splitting and gradient calculation methods were the same as those used for the full three dimensional computations. In addition, an implicit axisymmetric density based compressible RANS solver was used. The computational mesh was generated using a fully structured blocked approach and the same blocking methodology as used in 3D was followed as closely as possible. Three meshes were created with element counts of 228,000, 119,000 and 62,000. As was the case for the 3D mesh refinement study, the mesh refinement was completed through a uniform decrease of the mesh node count in the radial and axial directions. Moreover, the first cell height was constant between the three meshes in order to ensure the same treatment of the wall boundaries. The results presented in sections III.C and III.D were computed using the 228,000 element mesh, which is shown in (Fig. 3b). As was the case for the 3D meshes, the initial cell height normal to the nozzle aerolines was set such that the value of y^+ was less than 1 across all of the aerodynamic conditions investigated. Each computation was manually inspected in order to ensure that this y^+ condition was met.

E. Effective Nozzle Pressure Ratio

Both the bypass and core nozzles will experience alterations to their operating point relative to the prescribed operating point due to external flow conditions. In order to quantify this suppression effect, an effective nozzle

pressure, NPR_e, has been defined for the bypass and core streams, Eq. (34) and (35). Where p_{19-te} is the circumferentially averaged static pressure at the trailing edge of the fan cowl.

$$FNPR_e = \frac{P_{13}}{p_{19-te}} \qquad (34)$$

$$CNPR_e = \frac{P_7}{p_{19-te}} \qquad (35)$$

As the freestream Mach number is varied, flow over the DSFRN fan cowl will result in a static pressure at the fan cowl trailing edge which is not equal to the ambient static pressure. As a result for this geometry, the local static pressure into which the bypass nozzle discharges into is not ambient and therefore the effective operating point of the bypass nozzle has been altered.

The static pressure at the trailing edge of the cowl is a function of the freestream Mach number, fan cowl geometric parameters, and the total pressure of the bypass flow. Therefore, $FNPR_e$ is implicitly linked to $FNPR_p$ due to the interaction between the flow over the fan cowl and the bypass nozzle jet. In order to quantify the relationship between $FNPR_p$ and $FNPR_e$, a linear regression analysis was completed between the two variables. As a result, the coefficient of determination [41], R^2, and gradient, $\frac{d(FNPR_e)}{d(FNPR_p)}$, have been calculated. The coefficient of determination provides a quantitative measure of how appropriate the linear regression analysis is [41]. Values of R^2 lie between 0 and 1 where a value of 0 indicates no correlation and a value of 1 indicates perfect correlation.

Suppression of the core nozzle flow arises due the presence of the bypass jet preventing the expansion of the core nozzle flow to the ambient static pressure in the nozzle near-field region. The static pressure into which the core nozzle discharges is therefore strongly dependent upon the state of the bypass jet and hence $FNPR_p$. As such, it is plausible to define an effective $CNPR_e$ relative to the static pressure at the trailing edge of the core cowl. However, this value of static pressure has a highly non-linear and non-monotonic relationship with the $FNPR_p$ at supercritical $FNPR_p$ due to the shape of the expansion and compression fans which form in the supersonic bypass jet. Instead the static pressure used in the effective $CNPR_e$ was taken at the fan cowl trailing edge. As a result, the suppression of the bypass jet due to the freestream is accounted for and the suppression from the bypass stream on the core flow will now primarily be a function of the extraction ratio, ER. In addition, the same linear regression analysis as was described for $FNPR_p$ and $FNPR_e$ was completed for $CNPR_p$ and $CNPR_e$.

Reduced order model for core discharge coefficient

In order to quantify the validity of the proposed effective $CNPR_e$ as a measure of suppression, a Reduced Order Model (ROM) was created based on the computed discharge coefficients from the axisymmetric simulations. An exponential function was chosen to model C_D^{Core} based on the asymptotic nature of C_D^{Core} with $CNPR_e$. The function had three variables which took the form of a constant (ζ), an exponent weight factor (λ), and an exponent (ξ), Eq. (36). A Root Mean Square Distance ($RMSD_{ROM}$) has been defined in order to quantify the accuracy of this model, Eq. (37). Where C^{CFD} is the value of the coefficient obtained from CFD analysis, C^{ROM} is the value predicted from the model and N is the number of data points at constant ER used to construct the model. The values for the three constants in Eq. (36) were chosen for each ER to minimize $RMSD_{ROM}$.

$$C_D^{Core} = \zeta - \lambda e^{-\xi CNPR_e} \tag{36}$$

$$RMSD_{ROM}(\%) = \sqrt[2]{\frac{1}{N}\sum_N \left(\frac{C^{CFD} - C^{ROM}}{C^{CFD}}\right)^2} \tag{37}$$

Linear regression analysis for the bypass and core gauge stream force

To account for the variations in both the bypass and core nozzle gauge stream force, a reduced order model was constructed based on results from the axisymmetric approach. F_{G19}^x was assumed to be a linear function of only the nominal $FNPR_p$ and linear regression analysis was used to calculate the resultant gradient, $\frac{d(F_{G19}^x)}{d(FNPR_p)}$, and $R_{F_{G19}^x,FNPR_p}^2$. F_{G9}^x was assumed to be a linear function of both $CNPR_p$ and ER. As with the bypass nozzle, the resultant gradient at constant ER, $\left.\frac{d(F_{G9}^x)}{d(CNPR_p)}\right|_{ER=const}$, and $R_{F_{G9}^x,CNPR_p}^2$ were calculated.

III.Results and Discussion

The results presented with this work can be broadly split into two sections: the verification and validation of the outlined numerical approaches and an exposition of the effect of external flow conditions on exhaust system performance. The Grid Convergence Index (GCI) [29,30] for each numerical approach is given as well as a quantification of the effects of the computational domain on the non-dimensional coefficients. A comparison is then

drawn between the experimental measurements and computational nozzle performance metrics at static conditions. In addition, fundamental aerodynamic mechanisms responsible for the resultant nozzle performance metrics are explored. After the numerical approaches have been validated and verified, the effects of external flow conditions on the nozzle performance metrics are quantified and explained.

A. Computational Grid and Domain Independency Studies

For the 3D computations, at a $FNPR_p$ of 2.2 and freestream Mach number of 0.01, an increase of 0.1% in C_{Fx} was observed between the 20D and 40D domains. Between the 40D and 60D the increase in C_{Fx} was 0.06%. As a result the 60D domain size was used for all of the computations in this study. For C_{Fx}, a GCI of 0.02% was calculated between the 21.2 million element and 32.5 million element meshes, taking a safety factor (defined in [29,30]) of 1.25 throughout. Across the three mesh resolutions the value of C_D^{Bypass} was invariant up to four decimal places. Consequently, the calculated GCI did not lie in the asymptotic range as the variation between the meshes was so small. For C_D^{Core} a GCI of 0.44% was calculated between the 32.5 million element and 21.2 million element meshes. A larger variation was seen in C_D^{Core} compared to C_D^{Bypass} as the core nozzle is unchoked. In addition, the base pressure into which the core nozzle discharges is strongly dependent on the resolution of the expansion and compression fan in the bypass jet. The 3D computations presented in the subsequent sections have been completed using the medium meshes. In addition, computations from the coarse mesh are included for reference.

For the axisymmetric models at a $FNPR_p$ of 2.2 a GCI of 0.02% was calculated between the 119,000 and 228,000 element meshes for C_{Fx}. The values of GCI for C_D^{Bypass} and C_D^{Core} were found to be 0.01% and 0.05% respectively. The fine mesh has been used for all subsequent axisymmetric computations.

B. Validation of Computational Approaches

The results in this section present a comparison between the computed nozzle performance metrics and the experimental test data. The experimental results are the average values obtained from the multiple tests completed by Mikkelsen et al. [**Error! Bookmark not defined.**]. The computational results are presented in two ways: firstly, in terms of absolute values of the performance metrics and secondly, as a percentage difference between the numerical calculations and experimental measurements, Eq. (38). A further quantitative measure for the accuracy of

each numerical approach is the Root Mean Squared Distance of the CFD results from the experimental results across the pressure ratios tested, $RMSD_{Exp}$, Eq. (39), where N is the number of data points and C is a generic coefficient.

$$\Delta C(\%) = \left(\frac{C^{Exp} - C^{CFD}}{C^{Exp}}\right).100 \tag{38}$$

$$RMSD_{Exp}(\%) = \sqrt[2]{\frac{1}{N}\sum_N\left(\left(\frac{C^{Exp} - C^{CFD}}{C^{Exp}}\right).100\right)^2} \tag{39}$$

Axial Force Coefficients

From a $FNPR_p$ from 1.4 to 2.4 C_{Fx} was experimentally found to be an increasing monotonic function with $FNPR_p$ (Fig. 4a). After a $FNPR_p$ of 2.4 C_{Fx} proceeded to decrease. This reduction arose due to increased shock losses over the core cowl. The 3D computations from this work were able to predict this increase in shock strength and subsequent decrease in C_{Fx} (Fig. 4a). The cause of the increased shock losses can be observed as with increased $FNPR_p$, from 2.4 to 2.8 as there is a concurrent increase in the pre-shock Mach number at the trailing edge of the core cowl (Fig. 5).Over a range of $FNPR_p$ from 1.4 to 2.8 $RMSD_{Exp}$ for C_{Fx} was found to be 0.02% for the coarse mesh and 0.03% for the medium mesh. For the coarse mesh the greatest deviation from the experimental data arose at a $FNPR_p$ of 2.4 with a value of ΔC_{fx} of -0.04% (Fig. 4b). From the second PAW values of ΔC_{fx} ranged from under predictions of 1.4% to over predictions of 0.3% and an average under prediction of 0.5% (Fig. 4b). As such, the predictions from all the numerical approaches in this study lie within the bounds of PAW2. It should be noted that as the ideal thrust used in the definition of C_{Fx} is based on the computed mass flows small discrepancies between the computational and experimental C_D^{Bypass} and C_D^{Core} should have a small impact on ΔC_{fx}.

The axisymmetric model was able to resolve the correct trend of the C_{Fx} characteristic with $FNPR_p$, but consistently over predicted C_{Fx} (Fig. 4a) with an $RMSD_{Exp}$ value of 0.36%. At a $FNPR_p$ of 1.4 the deviation was 0.52% which reduced to 0.26% at a $FNPR_p$ of 2.8 (Fig. 4b). This over prediction arose due to the lack of $\theta_{pylon-wet}$ and $\phi_{pylon-dry}$ (Fig. 1 and Eq. (15)) in the axisymmetric calculations. This indicates that the axisymmetric approach is valid for observing trends but not for predicting the absolute values of the performance metrics.

Discharge Coefficients

At a $FNPR_p$ of 1.4 the bypass nozzle is unchoked, and with increased $FNPR_p$ C_D^{Bypass} reaches its asymptotic value once the bypass nozzle chokes at a $FNPR_p$ between 1.8 and 2.0 (Fig. 4c). Above a $FNPR_p$ of 2.0, a minor increase of C_D^{Bypass} occurs (Fig. 4c). This arises as the increased $FNPR_p$ is achieved by increasing the inlet total pressure; thus, the bypass nozzle Reynolds number will increase which serves to reduce boundary layer growth within the bypass nozzle. The coarse and medium 3D meshes calculated a $RMSD_{Exp}$ of 0.37% and 0.36% respectively for C_D^{Bypass}. There was a slight increase in ΔC_D^{Bypass} with increased $FNPR_p$ as the nozzle choked but this was minimal (Fig. 4d). For the medium mesh ΔC_D^{Bypass} decreased from -0.53% to -0.45% between a FNPR of 1.4 and 2.8 (Fig. 4d). This improvement in ΔC_D^{Bypass} prediction can be attributed to the bypass nozzle choking and hence the nozzle became insensitive to variations in the downstream conditions. As the nozzle is choked the CFD prediction is more accurate as the behavior of the downstream shear layer and shock losses have a negligible effect on the bypass flow. As opposed to the unchoked case where static pressure variations due to the mixing of the freestream and bypass jet propagate into the bypass duct. Given that the values of ΔC_D^{Bypass} from PAW2 range from -1.4 to +0.25%, the value of ΔC_D^{Bypass} of -0.37% for medium mesh is considered a good result.

The axisymmetric model was found to calculate C_D^{Bypass} to within 0.04% of the experimental value across all of the $FNPR_p$ investigated (Fig. 4c) with a $RMSD_{Exp}$ of 0.02%. The very low values of $RMSD_{Exp}$ that result from the axisymmetric model are erroneous as the flow blockage due to boundary layer growth on the upper and lower bifurcation and bifurcation end-wall effects are cannot be modelled with such a simplified approach. However, from the axisymmetric results it can be concluded that the variation of C_D^{Bypass} with increased $FNPR_p$ is mostly governed by 2D loss mechanisms.

A much larger variation of C_D^{Core} was observed over the range of $CNPR_p$ investigated compared with C_D^{Bypass}. For example, over a $CNPR_p$ from 1.17 to 2.34, C_D^{Core} increased from 0.80 to 0.97 (Fig. 4e). This larger variation is due to the suppression of the core stream by the fan stream. The fan stream impedes the expansion of the core jet and expansion and compression waves in the fan jet alter the back pressure downstream of the core nozzle. Consequently, the behavior of C_D^{Core} is a function of both $CNPR_p$ and $FNPR_p$. An example of this dependency occurs at a $CNPR_p$ between 1.80 and 2.34 (Fig. 4e). From a $CNPR_p$ of 1.80 to 2.20 C_D^{Core} decreases monotonically

from 0.94 to 0.93, but at a $CNPR_p$ of 2.34 there is a rise in C_D^{Core} to 0.96 (Fig. 4e). This increase occurs due to changes in the bypass jet shock topology on the core cowl. As the strength of the bypass jet shock increases between a $CNPR_p$ of 2.20 and 2.34 (a change in $FNPR_p$ from 2.6 to 2.8) the core cowl boundary layer undergoes a shock induced separation at the trailing edge (Fig. 5). As a result the shock moves upstream, reducing the static pressure at both the core cowl trailing edge and core nozzle throat and therefore increasing the mass flow rate through the core nozzle. This feature is shown by both the 3D and axisymmetric computations. For the 3D computations $RMSD_{Exp}$ values of ΔC_D^{Core} were 0.41% and 0.31% for the coarse and medium meshes respectively with the maximum value of ΔC_D^{Core} equal to -0.7% at a $CNPR_p$ of 2.16 for both meshes (Fig. 4f). An increase of $|\Delta C_D^{Core}|$ with $CNPR_p$ was observed for both of the computational approaches used in this study and in the average values from PAW2 (Fig. 4f).

The $RMSD_{Exp}$ for the medium mesh of three dimensional approach discussed above has been shown to lie within the range of those reported in the second PAW, with values of 0.03%, 0.37% and 0.40% across a range of $FNPR_p$ from 1.4 to 2.8 for C_{Fx}, C_D^{Bypass} and C_D^{Core} respectively. The axisymmetric approach was shown to resolve the trends of each nozzle performance metric across a range of $FNPR_p$, and as a result it has been used to explore the sensitivity of the nozzle performance metrics to freestream Mach number and ER in the subsequent sections. The use of this model allows a larger range of operating conditions to be investigated, as typically considered within a preliminary design stage.

C. The effect of external flow conditions on nozzle discharge coefficients

Bypass Flow Suppression

As discussed in section II.F, flow over the fan cowl will result in the alteration of operating point of the bypass nozzle. For all of the operating conditions investigated, a strong linear relationship between the proposed effective $FNPR_e$ and the nominal $FNPR_p$ was found; with a product moment correlation coefficient, $R_{FNPR_e,FNPR_p}$, of at least 0.9996. As such, for this geometry it can be deduced that the interaction of the fan cowl and bypass jet is a linear function of $FNPR_p$. In the case of both the static conditions and at a Mach number of 0.3, $\frac{d(FNPR_e)}{d(FNPR_p)}$ are very close to 1 with values of 1.00 and 0.998 respectively. This occurs as there is very little change in the static pressure

at the trailing edge of the cowl across the range of $FNPR_p$ from 1.4 to 2.8 for freestream Mach numbers of 0.01 and 0.3. However, at a Mach number of 0.85 $\frac{d(FNPR_e)}{d(FNPR_p)}$ decreases to 0.883. As a result of the increased static pressure at the fan cowl there is a concurrent increase in the static pressure along the bypass-jet post-exit streamtube (Fig. 7). No variation of $\frac{d(FNPR_e)}{d(FNPR_p)}$ with ER was observed relative to the values reported for an ER of 1.2. However at $FNPR_e$ less than 1.8, there are variations of C_D^{Bypass} with freestream Mach number (Fig. 6b).

As $\frac{d(FNPR_e)}{d(FNPR_p)}$ for both the Mach 0.01 and 0.3 cases were found to be close to 1 there is very little difference between the behavior of C_D^{Bypass} with both $FNPR_p$ and $FNPR_e$ (Fig. 6a and b). A minor deviation of less than 0.005 in C_D^{Bypass} was found at a $FNPR_p$ of 1.5 between the Mach 0.01 and 0.3 cases (Fig. 6a). For the Mach 0.85 case the largest deviation in C_D^{Bypass} from the static case was 0.08 and this occurred at $FNPR_p$ of 1.5, the lowest $FNPR_p$ simulated. This reduction in mass flow occurs as the higher static pressure along the fan cowl and post-exit streamtube prevents the bypass flow expanding to the ambient static pressure. As the bypass nozzle is unchoked these variations in static pressure propagate into the duct and increase the static pressure in the bypass nozzle at the higher Mach number compared with the static case.

In terms of $FNPR_p$, the choking point of the nozzle at a freestream Mach number of 0.85 increases to 2.3 compared to 2.0 in the static case (Fig. 6a). This change in choking point is due to the reduction of $\frac{d(FNPR_e)}{d(FNPR_p)}$ as a higher $FNPR_p$ is required to achieve the same $FNPR_e$. It is clear that at a $FNPR_e$ greater than 1.8 there is no influence of the M_{inf} on C_D^{Bypass} as all three of the nozzle characteristics reduce to one curve (Fig. 6b). When $FNPR_e$ is below 1.8 significant differences in C_D^{Bypass} between the three Mach numbers are observed. From a design perspective, above a $FNPR_e$ of 2.0 C_D^{Bypass} can be assumed to be a function of $FNPR_e$ only, therefore the variation C_D^{Bypass} with $FNPR_e$ at static test conditions can be used to size the bypass nozzle throat area at cruise conditions.

Core flow suppression

A similar analysis as presented for the bypass nozzle can be applied to the core nozzle. Due to the use of p_{19-TE} to define $CNPR_e$, see Eq. (35), $\frac{d(CNPR_e)}{d(CNPR_p)}$ will be identical to $\frac{d(FNPR_e)}{d(FNPR_p)}$. Across the range of operating conditions investigated the area-weighted static pressure at the core nozzle throat did not reach an asymptotic value and

therefore it can be concluded that the core nozzle did not choke. Therefore, much larger variations to C_D^{Core} compared with C_D^{Bypass} are expected.

With increased ER there is a marked decrease in the maximum C_D^{Core} achieved (Fig. 8a, c and e). The maximum values of C_D^{Core} were found to be 0.96, 0.88 and 0.82 for ERs of 1.2, 1.4 and 1.6, respectively (Fig. 8a, c and e). Across the range of ERs investigated there is very little difference between C_D^{Core} at Mach numbers of 0.01 and 0.3 with the C_D^{Core} from the 0.3 cases at a constant offset from the values at 0.01 (Fig. 8a, c and e). This occurs due to the similar values of $\frac{d(FNPR_e)}{d(FNPR_p)}$ and hence $\frac{d(CNPR_e)}{d(CNPR_p)}$ between the Mach 0.01 and 0.3 cases. However, a much larger difference in C_D^{Core} occurred at the freestream Mach number of 0.85, particularly at $CNPR_p$ of less than 2.0 (Fig. 8a, c and e). For example, at a $CNPR_p$ of 1.5, C_D^{Core} has reduced by 0.09 for extraction ratios of 1.2 and 1.6, respectively, compared with the static cases.

The 0.01 and 0.3 Mach cases exhibit a non-monotonic variation of C_D^{Core} with $CNPR_p$ between $CNPR_p$ of 1.6 and 2.0 across all the ERs investigated and is most notable at ERs of 1.4 and 1.6 (Fig. 8a, c and e). These non-monotonic changes occur as the local static pressure which the core nozzle discharges into is dependent on the expansion and compression waves present in the bypass jet. The increased pressure at the fan cowl trailing edge at a Mach number of 0.85 serves to increase the average static pressure along the core streamline and hence produce a smoother static pressure distribution across the core streamline (Fig. 7). As the core nozzle is unchoked the expansion of the flow is highly dependent on such variations in static pressure. These effects make the correlation of C_D^{Core} with $CNPR_p$ more difficult compared with the correlation of C_D^{Bypass} with $FNPR_p$.

If the postulation that the suppression of C_D^{Core} is only a function of $CNPR_e$ and ER is correct, then the C_D^{Core} nozzle characteristic with $CNPR_e$ at various freestream Mach numbers should be a unique relationship. It can be seen from Fig. 8b,d and f that this is not the case as the Mach 0.85 characteristic is different from the of the lower Mach number configurations. Quantitatively this is shown by the value of $RMSD_{ROM}$ which was defined in Eq. (37). For ERs of 1.2, 1.4 and 1.6 $RMSD_{ROM}$ took values of 0.28, 0.72, and 1.12% respectively. Evidently, at higher values of ER the influence that both the freestream Mach number and bypass jet have on C_D^{Core} is larger.

The constant ζ used in the model of Eq. (36) has a clear physical meaning as it corresponds to the asymptotic value of C_D^{Core} and serves to quantify the maximum C_D^{Core} which could be achieved for a given ER at large values of $CNPR_e$. The relationship between α and ER was found to be a negative linear correlation ER (Table 1). If a nozzle

was intended to operate at multiple ERs, a robust nozzle design would aim to minimize $\frac{d\zeta}{dER}$ in order to reduce the impact of ER on the maximum achievable C_D^{Core}. Both λ and ξ were found to be to be non-linear monotonic functions of ER, Table 1 . As a result, at higher ER the asymptotic value of C_D^{Core} will be reached at lower values of $CNPR_e$. The constants from this correlation serve to quantify the effect of flow suppression on C_D^{Core} and give an indication of the off-design performance for a given nozzle geometry. With correlations for C_D^{Core} as a function of $CNPR_e$ and ER, estimation of the required core nozzle throat area for a given cycle can be made. In addition, the effect of off-design operations on engine performance could be investigated by coupling the correlations to an engine performance code.

The discussion in the preceding section has shown that both $FNPR_e$ and $CNPR_e$ provide quantification for the changes in the nozzle operating point of a nozzle due to external flow conditions. Suppression of C_D^{Core} was found to be a strong function of ER with the asymptotic value of C_D^{Core} found to decrease linearly with ER. The proposed reduced order model for C_D^{Core} was unable to capture the non-monotonic variation in C_D^{Core} due to the formation of shock waves in the bypass jet. For the bypass nozzle, it was shown that measurements of C_D^{Bypass} from static tests conditions are sufficient to size the bypass nozzle area. However, due to fact that $\frac{d(FNPR_e)}{d(FNPR_p)}$ will be less than one at cruise conditions, an estimate of $FNPR_e$ is required to ensure that bypass nozzle will indeed operate at choked conditions. In addition to suppression of the bypass and core nozzles mass flows, the sensitivity of the non-dimensional force and thrust coefficients to external flow conditions needs to be investigated.

D. Force and Thrust Coefficients

With increased Mach number an increase in C_V^* is observed across a range of $FNPR_p$ from 1.4 to 2.8, (Fig. 9a). An increased C_V^* occurs with non-zero freestream Mach numbers relative to the static cases due to an increased pressure force on the core cowl and core plug afterbodies at the non-static cases. Furthermore, $p_{cowl-TE}$ was found to be greater than ambient for the cases with freestream flow (Fig. 7). This increase in static pressure served to reduce strength of the shock wave located at the trailing edge of the core cowl. For example, at a $FNPR_p$ of 2.6 and ER of 1.6 the minimum pressure coefficient ($\frac{p-p_{atm}}{p_{atm}}$) on the core cowl reduces from -0.2 to 0.05 as the freestream Mach number is increased from 0.01 to 0.85 (Fig. 7). The increase in C_V^* with flight Mach number is counteracted by

an increased drag on the fan cowl, as shown by a lower C_{Fx} with increased Mach number (Fig. 9b). The extraction ratio (ER) was found to have greatest influence on both C_{Fx} and C_V^* at a freestream Mach number of 0.85 (Fig. 9b).

The axial gauge stream force at the throat of the bypass nozzle, F_{G19}^x, was found to be a linear function of $FNPR_p$ with a value of $R^2_{F_{G19}^x, FNPR_p}$ of 0.9994 across all of the Mach numbers investigated. Therefore, the suppression of the bypass flow from the freestream had a negligible effect on the internal duct pressures losses. Furthermore, the axial gauge stream force at the throat of the core nozzle, F_{G9}^x, was found to be a linear function of $CNPR_p$ at a given ER for all of the Mach numbers investigated. The value of $R^2_{F_{G9}^x, CNPR_p}$ decreased with ER, although a strong linear correlation was still obtained with a $R^2_{F_{G9}^x, CNPR_p}$ of greater than 0.99 across the range of ER. The magnitude of the bypass suppression onto F_{G9}^x can be quantified by the gradient of F_{G9}^x with $CNPR_p$, $\frac{d(F_{G9}^x)}{d(CNPR_p)}$, with lower gradients indicative of a greater suppression effect. A non-monotonic variation of $\frac{d(F_{G9}^x)}{d(CNPR_p)}$ with ER was found. The largest values of $\frac{d(F_{G9}^x)}{d(CNPR_p)} \bigg/ \frac{d(F_{G9})}{d(CNPR_p)}\bigg|_{ER=1.2}$ occurred at an ER of 1.4 with the smallest at 1.6. with values of 1.03 and 0.988 respectively. This variation of F_{G9}^x suppression does not follow the same relationship as was followed by the suppression of C_D^{Core}.

IV. Conclusions

Within this work two computational models for the prediction of the aerodynamic performance of a separate-jet exhaust system have been developed and validated against experimental measurements of non-dimensional performance metrics. For the three dimensional approach containing 21.2 million elements the RMS deviation from the experimental data was found to be 0.03%, 0.37% and 0.31% for the thrust coefficient, bypass discharge coefficient and core discharge coefficient respectively. The simplified two-dimensional axisymmetric model for the DSFRN was found to correctly predict the same trends in nozzle performance metrics as the full 3D computations and has been used to explore the sensitivity of nozzle performance metrics to freestream Mach number and extraction ratio.

The effective nozzle pressure ratio was found to be a key parameter in the quantification of flow suppression for both the bypass and core nozzles. A reduced order model for the core discharge coefficient based upon the effective nozzle pressure ratio and extraction ratio was created and shown to agree with CFD data over a range of Mach

numbers with an RMS deviation of between 0.28% and 1.12 %. Furthermore, the suppression of the core nozzle was found to be a strong function of extraction ratio; with the asymptotic value of the core discharge coefficient a negative linear function of extraction ratio. The greatest effect on the bypass nozzle was the reduction of the effective nozzle pressure ratio with increasing Mach number due to flow over the fan cowl with the lower the prescribed fan nozzle pressure ratio the greater this effect.

When subject to non-zero freestream Mach numbers the behavior of the modified thrust coefficient was dominated by changes on the exhaust afterbody forces. The aerodynamic mechanisms which govern the performance of separate-jet exhaust systems have been identified, quantified, and correlated to fundamental aerodynamic parameters. Consequently, both quantitative and qualitative assessments of exhaust system performance with freestream Mach number and extraction ratio relative to static conditions can be made.

Acknowledgments

References

[1] Birch, N. T., "2020 Vision: The Prospects for Large Civil Aircraft Propulsion", *The Aeronautical Journal*, Vol.104, Issue 1038, 2000, pp. 347-352.

doi:10.1017/S0001924000063971

[2] Guha A., "Optimum Fan Pressure Ratio for Bypass Engines with Separate or Mixed Exhaust Streams", *Journal of Propulsion and Power*, Vol.17, No.5, 2001, pp. 1117-1122.

doi: 10.2514/2.5852

[3] Goulos I., Stańkowski T., Otter J., MacManus D., Grech N. and Sheaf C., "Aerodynamic Design of Separate-Jet Exhausts for Future Civil Aero-engines—Part I: Parametric Geometry Definition and Computational Fluid Dynamics Approach", *Journal of Engineering for Gas Turbines and Power,* Vol. 138, Issue 8, Paper No: GTP-15-1538, 2016.

doi: 10.1115/1.4032649

[4] Mattingly J. D., *Elements of Gas Turbine Propulsion: Gas Turbines and Rockets*, AIAA Education Series, AIAA, Virginia, 2006, pp.727.

[5] DeBonis J. R., "Gas Turbine Engines: Nozzles", *Encyclopedia of Aerospace Engineering*.

doi: 10.1002/9780470686652.eae096

[6] de Wolf W. B, "Possibilities and limitations of VHBR and UHBR Turbofan Simulations in Engine/Airframe Integration Wind Tunnel Experiments", *Proceedings of the DLR Workshop: Aspects of Engine-Airframe Integration for Transport Aircraft*, DLR Mitteilung, 1996, pp 21-1 - 21-18.

[7] Geyr, H. and Rossow, C., "A Correct Thrust Determination Method for Turbine Powered Simulators in Wind Tunnel Testing", AIAA-Paper 2005-3707, 2005.

doi: 10.2514/6.2005-3707

[8] Odbert, E., *Aerodynamic Design of Transport Aircraft*, Delft University Press, The Netherlands, 2009, pp 505.

[9] Harris, A. E. and Paliwal, K. C., "Civil Turbofan Propulsion System Integration Studies using Powered Testing Techniques at ARA, Bedford", AIAA Paper-84-0593, 1984.

[10] Georgiadis N. J. and DeBonis J. R., "Naiver-Stokes Analysis Methods for Turbulent Jet Flows With Application To Aircraft Exhaust Nozzles", *Progress in Aerospace Sciences,* Vol. 42, Issues 5-6, 2006, pp. 377-418.

doi:10.1016/j.paerosci.2006.12.001

[11] Keith B. D., Uenishi K. and Dietrich D. A. "CFD-Based Three-Dimensional Turbofan Exhaust Nozzle Analysis System*", Journal of Propulsion and Power*, Vol.9, No.6, 1993, pp. 840-846.

doi: 10.2514/3.23698

[12] Abdol-Hamid K. S., Keith B. D., Uenishi K. and Carlson J. R., "Commercial Turbofan Engine Exhaust Nozzle Flow Analyses", *Journal of Propulsion and Power,* Vol.9, No.3, 1993, pp. 431-436.

doi: 10.2514/3.23639

[13] Massey S. J., Thomas R. H., Abdol-Hamid K. S. and Elmiligui A. A., "Computational and Experimental Flowfield Analyses of Separate Flow Chevron Nozzles and Pylon Interaction", AIAA Paper 2003-3212, 2003.

[14] Sloan B., Wang J., Spence S., Raghunathan S. and Riordan D., "Aerodynamic Performance of a Bypass Engine with Fan Nozzle Exit Area Change by Warped Chevrons", IMechE Journal of Aerospace Engineering, Vol. 224, (6), January 2010, pp.731 -73

[15] Malecki R. and Lord W. K., "Aerodynamic Performance of Exhaust Nozzles Derived from CFD simulation", AIAA Paper 1995-2623, 1995.

[16] Hsiao E., Su M. W. and Colehour J. L., "Navier-Stokes Analysis of a High By-pass Engine Exhaust System and Plume", AIAA Paper 1997-2282, 1997.

[17] Dembowski M. A. and Georgiadis N. J., "An Evaluation of Parametric Influencing Jet Mixing Using the WIND Navier-Stokes Code", NASA TM-2002-211727.

[18] Abdol-Hamid K. S., Paul Pao S., Massey S. J., Elmiligui A., "Temperature Corrected Turbulence Model for High Temperature Jet Flow", AIAA Paper 2003-4070, 2003.

[19] Viswanathan K., Spalart P. R., Czech M. J., Garbaruk A. and Shur M., "Tailored Nozzles for Jet Plume Control and Noise Reduction", AIAA Journal, Vol. 50, No. 10, October 2012, pp 2115- 2134

[20] Thornock R. L. and Sokhey J., "Propulsion Aerodynamics Workshop I, Comparison of Participant Analyses With Experimental Results For Convergent Conical Nozzles Flow Fields And Performance", AIAA Paper 2013-3735, 2013.

doi: 10.2514/6.2013-3735

[21] Domel N. D, "Perspectives on Propulsion CFD for Nozzle Applications Relevant to the AIAA Propulsion Aerodynamics Workshop", AIAA Paper 2015-3778, 2015.

doi: 10.2514/6.2015-3778

[22] Li Z., Chen H., Zhang "NSAWET Results of the Dual Separate Flow Reference Nozzle From AIAA PAW02", AIAA Paper No. 2015-3779, 2015.

doi:10.2514/6.2015-3779

[23] Zhang, Y.F., Chen, H.X., Zhang, M., Zhang, M.H., and Li, Z., et al., "Performance Prediction of Conical Nozzle Using Navier-Stokes Computation," *Journal of Propulsion and Power*, Vol. 31, No. 1, 2015, pp. 192-203.

doi: 10.2514/1.B35164

[24] Spotts N., Guzik S. and Gaoz X., "A CFD Analysis of Compressible Flow Through Convergent-Conical Nozzles", AIAA Paper 2013-3734, 2013.

doi:10.2514/6.2013-3734

[25] Thornock, R. L. "Propulsion Aerodynamics Workshop IIL Participants' Analyses of A Dual Separate Flow Reference Nozzle in Terms of Thrust and Flow Performance", AIAA Paper No. 2016-4503, 2016.

[26] Mikkelsen, K. L., Myren, D. J., Dahl D. G. and Christiansen, M. D, "Initial Subscale Performance Measurements of the AIAA Dual Separate Flow Reference (DSFR) Nozzle", AIAA Paper No. 2015-3883, 2015.

doi:10.2514/6.2015-3883

[27] Compton W. B., "Effects of Jet Exhaust Gas Properties on Exhaust Simulation and Afterbody Drag", NASA TR R-444.

[28] MIDAP Study Group, "Guide to In-Flight Thrust Measurement of Turbojets and Fan Engines", *Advisory Group for Aerospace Research and Development* , AGARDograph No.237, Paris, 1979

[29] Roache, P.J., "Perspective: A Method For Uniform Reporting Of Grid Refinement Studies", *Journal of Fluids Engineering*, Vol. 116, No. 3, 1994, pp. 405-413.

doi:10.1115/1.2910291

[30] Roache, P. J., "Quantification of Uncertainty in Computational Fluid Dynamics", *Annu. Rev. Fluid. Mech.*, Vol. 29, 1997, pp. 129-160.

doi: 10.1146/annurev.fluid.29.1.123

[31] Wilcox D.C., "Effects of Compressibility", *Turbulence Modeling for CFD*, 3rd ed., DCW Industries, Inc., California, 2006, pp. 243 – 255.

[32] Menter, F. R., "Two-Equation Eddy-Viscosity Turbulence Models for Engineering Applications", *AIAA Journal*, Vol. 32, No. 8, 1994, pp. 1598–1605.

doi: 10.2514/3.12149

[33] Walsh, P., and Fletcher, P., "Properties and Charts for Dry Air, Combustion Products and other Working Fluids", *Gas Turbine Performance,* 2nd ed., Blackwell Publishing, Oxford, 2004, pp. 115.

[34] ANSYS Inc, "ANSYS FLUENT Theory Guide: Release 15.0", ANSYS, Inc., Canonsburg, PA,2013.

[35] Sutherland, W., "The Viscosity of Gases and Molecular Forces", *Philosophical Magazine*, Vol. 5, No. 36, 1893, pp 507-531.

[36]Weiss, J. M., Maruszewski, J. P. and Smith, W. A., "Implicit Solution of the Navier-Stokes Equations on Unstructured Meshes", AIAA Paper 97-2103, 1997.

doi:10.2514/6.1997-2103

[37] Weiss, J. M. and Smith, W.A., "Preconditioning Applied to Variable and Constant Density Flows", *AIAA Journal*, Vol. 33 No. 11, 1995, pp. 2050–2057.

doi: 10.2514/3.12946

[38] Holmes, D. G. and Connell, S. D., "Solution of the 2D Navier-Stokes Equations on Unstructured Adaptive Grids", AIAA Paper 89-1932, 1989.

doi:10.2514/6.1989-1932

[39] Rauch, R. D., Batira J. T. and Yang, N. T. Y., "Spatial Adaption Procedures on Unstructured Meshes for Accurate Unsteady Aerodynamic Flow Computations", AIAA Paper 91-1106, 1991.

doi:10.2514/6.1989-1932

[40] Roe, P. L., "Characteristic based schemes for the Euler equations", Annual Review of Fluid Mechanics, Vol. 18, January, 1986, pp. 337–365.

doi:10.1146/annurev.fl.18.010186.002005

[41] Montgomery, D. C, Runger G. C and Hubele N. F., "Building Empirical Models", *Engineering Statistics,* 3rd Ed., John Wiley and Sons, Inc., New York, 2004 , pp. 271
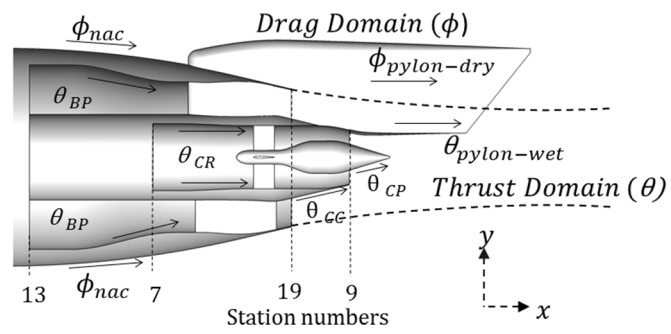
Figures

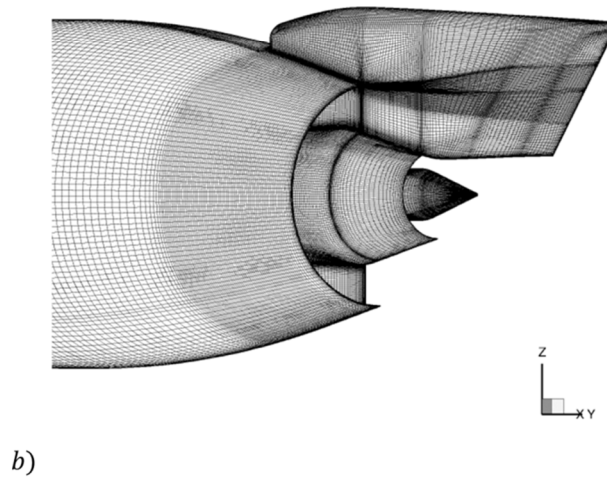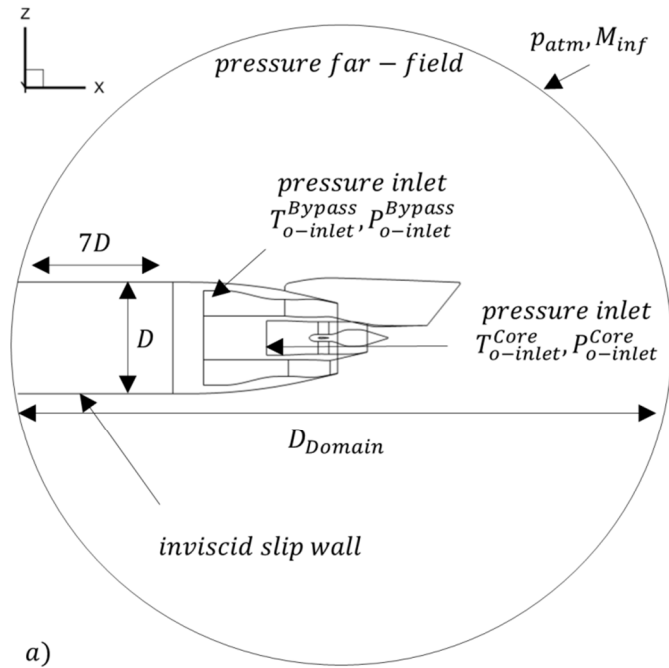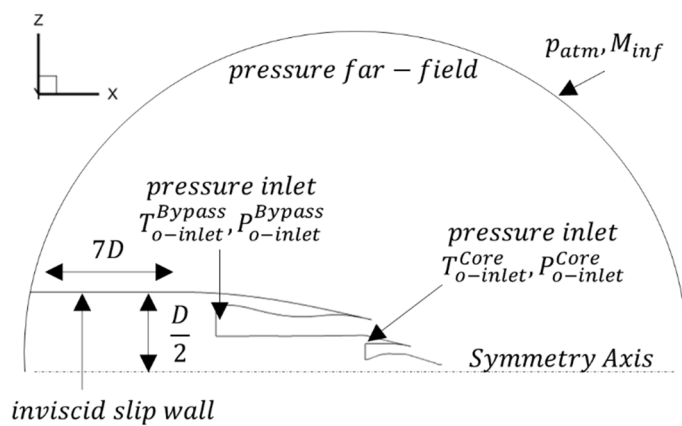

Fig. 1 Schematic for the breakdown of thrust and drag

a)

b)

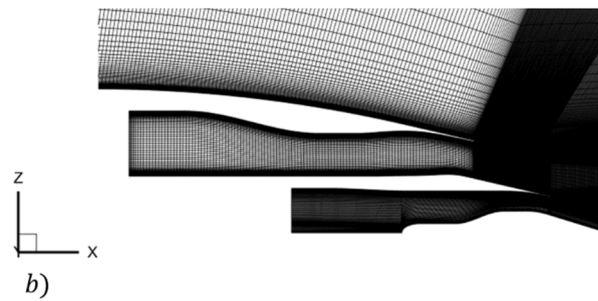**Fig. 2 (a) Boundary conditions and (b) surface mesh for 3D computations**

z

x

pressure far − field

p_{atm}, M_{inf}

pressure inlet
$T_{o-inlet}^{Bypass}, P_{o-inlet}^{Bypass}$

pressure inlet
$T_{o-inlet}^{Core}, P_{o-inlet}^{Core}$

7D

$\dfrac{D}{2}$

Symmetry Axis

inviscid slip wall

a)

z

x

b)

Fig. 3 (a) Boundary conditions and (b) mesh for axisymmetric calculations
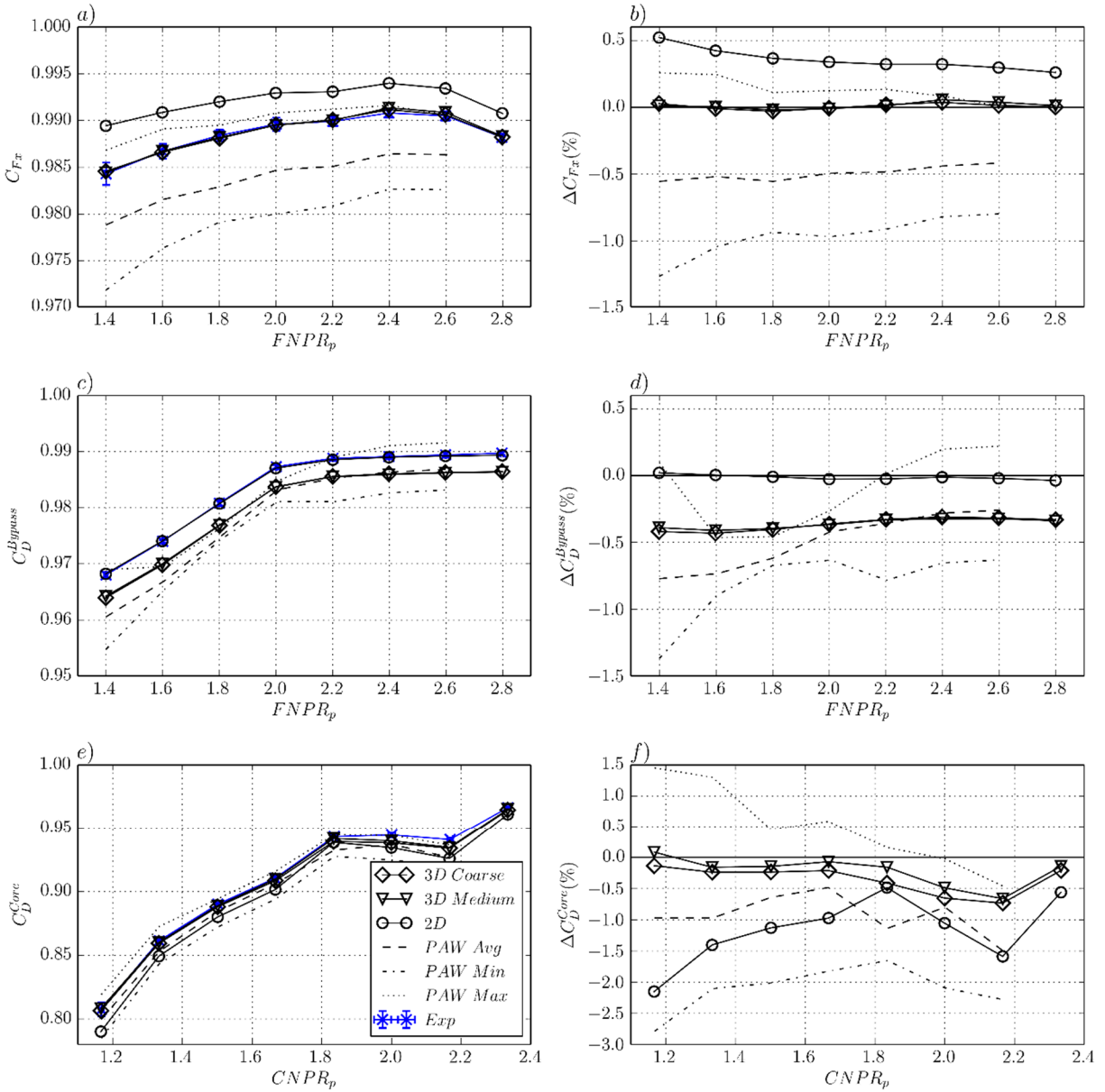
Fig. 4 Nozzle performance metrics from this study, experimental measurements [Error! Bookmark not defined.**], and PAW2 [21]**
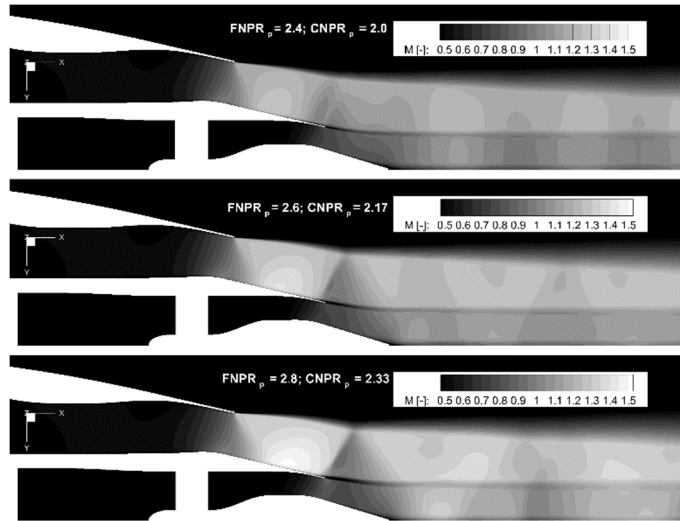
Fig. 5 3D Coarse Mesh Mach Number Contours at Z=0
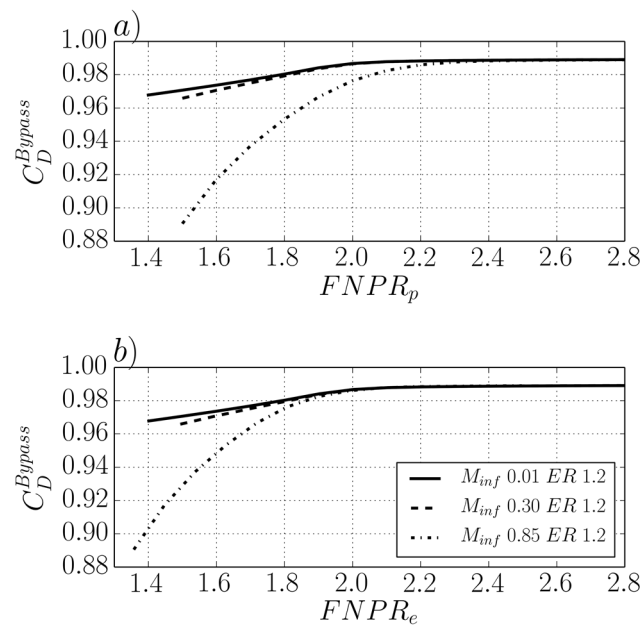
Fig. 6 Variation of C_D^{Bypass} **with a)** $FNPR_p$ **and b)** $FNPR_e$
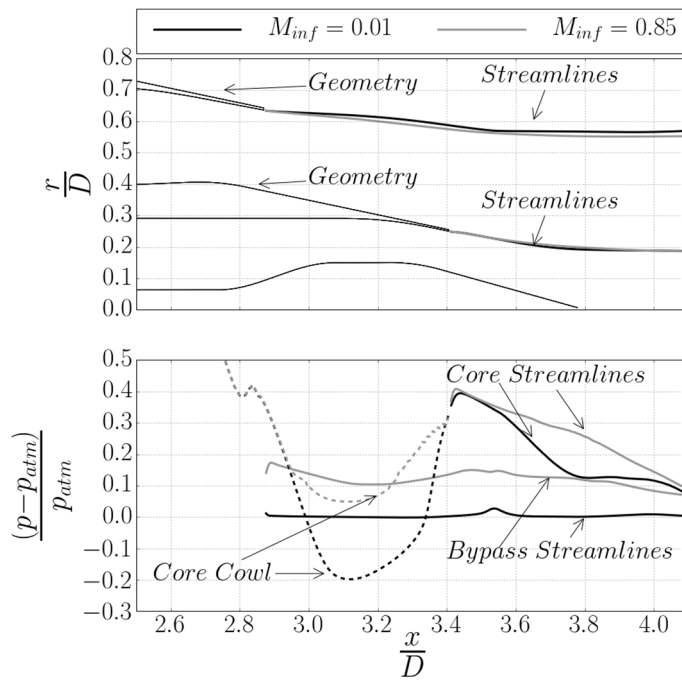
Fig. 7 Post-exit streamline and static pressure variation at FNPR = 2.6 and CNPR = 1.625

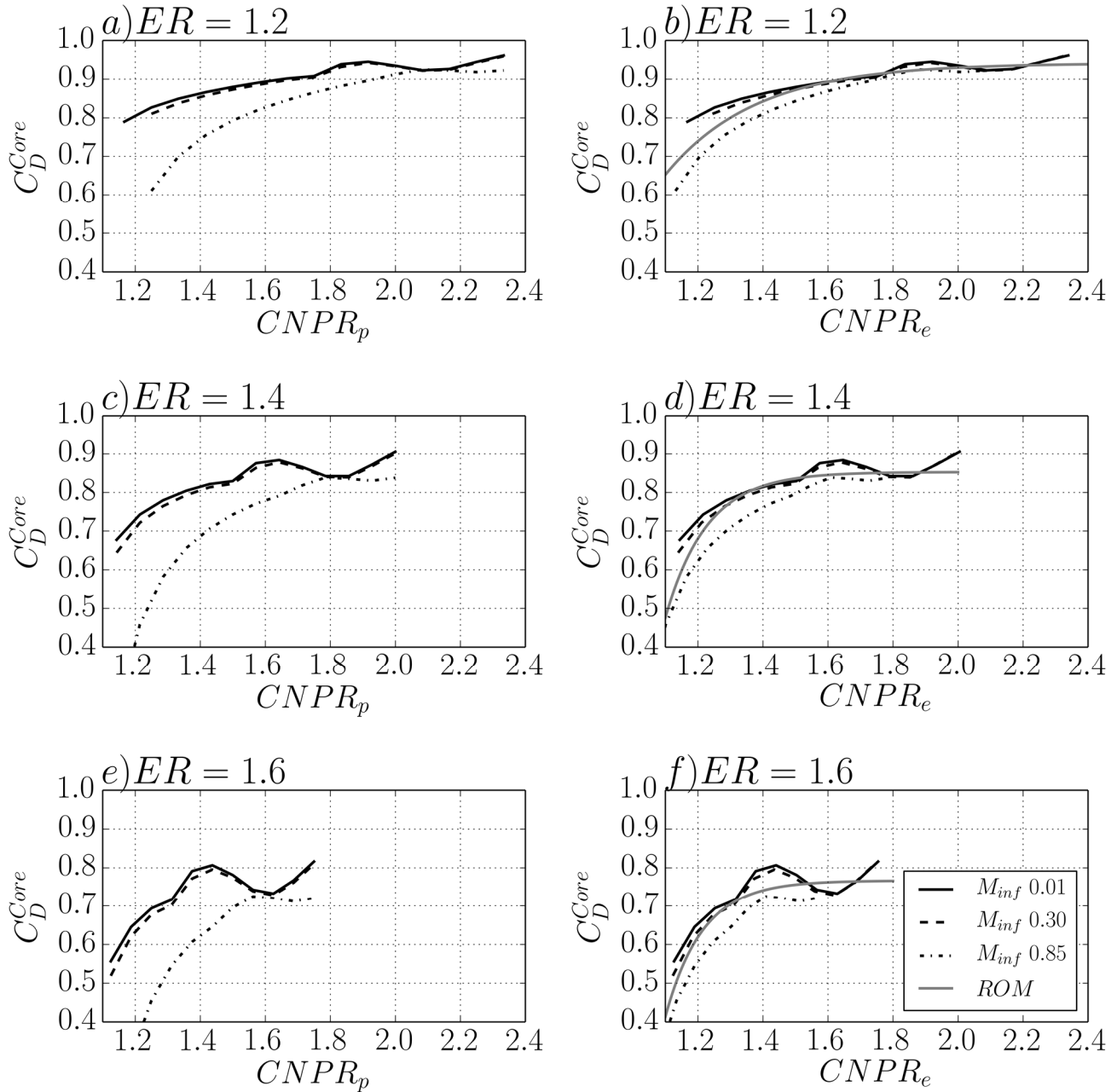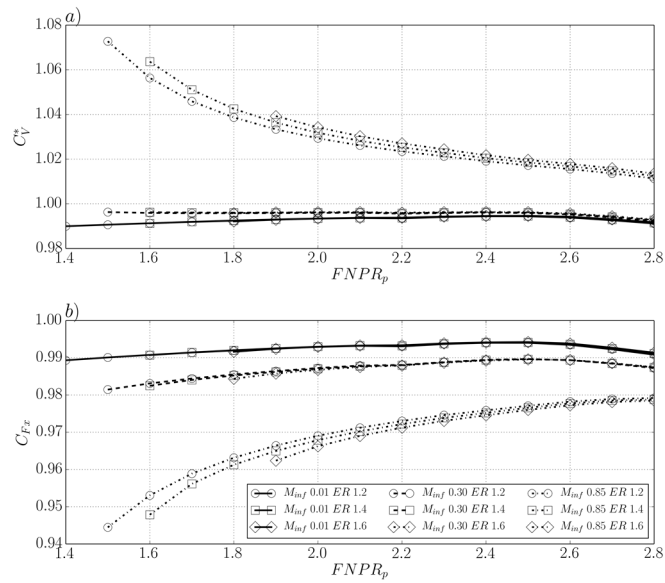**Fig. 8** Variation of C_D^{Core} with $CNPR_p$ and $CNPR_e$

Fig. 9 Variation of a) C_V^* and b) C_{Fx} with M_{inf}

Tables

Table 1 Variation of core discharge coefficient
exponential correlation variables with *ER*

ER	1.2	1.3	1.4	1.5	1.6
ζ	0.941	0.902	0.852	0.817	0.766
λ	14.7	127.339	1021	2038	5185
ξ	3.578	5.316	7.243	7.815	8.72